

Radial Mechanical Properties of Single-Walled Boron Nitride Nanotubes

Meng Zheng, Xiaoming Chen, In-Tae Bae, Changhong Ke,* Cheol Park, Michael W. Smith, and Kevin Jordan

The radial mechanical properties of single-walled boron nitride nanotubes (SW-BNNTs) are investigated by atomic force microscopy. Nanomechanical measurements reveal the radial deformation of individual SW-BNNTs in both elastic and plastic regimes. The measured effective radial elastic moduli of SW-BNNTs are found to follow a decreasing trend with an increase in tube diameter, ranging from 40.78 to 1.85 GPa for tube diameters of 0.58 to 2.38 nm. The results show that SW-BNNTs have relatively lower effective radial elastic moduli than single-walled carbon nanotubes (SWCNTs). The axially strong, but radially supple characteristics suggest that SW-BNNTs may be superior to SWCNTs as reinforcing additives for nanocomposite applications.

1. Introduction

Boron nitride nanotubes (BNNTs)^[1,2] are a type of one-dimensional nanostructure, composed of repeated and partially ionic B–N bonding networks. BNNTs possess extraordinary mechanical properties, thermal conductivity, and chemical stability, which are comparable, or even superior, to those of their pure carbon counterparts, carbon nanotubes (CNTs).^[3] A Young's modulus of BNNTs as high as 1.3 TPa has been reported.^[4–6] The thermal conductivity of BNNTs is predicted to be over $\approx 3000 \text{ W m}^{-1} \text{ K}^{-1}$.^[7] BNNTs are also very resistant to oxidation at high temperature (up to 800 °C) in air^[8] and inert to harsh chemicals.^[9] Unlike the semiconductive or metallic properties of CNTs, BNNTs possess a large bandgap ($\approx 5\text{--}6 \text{ eV}$ ^[1,10,11]) and thus are excellent electrical insulators. Applications of BNNTs include mechanical and/

or thermal reinforcing additives for polymeric and ceramic composites,^[12,13] protective shields/capsules,^[14] and electrical insulators. The radial elasticity of BNNTs is an important, but yet unexplored, issue for a complete understanding of their structural and material properties and the related applications. For instance, the radial rigidity of BNNTs is relevant to their structural configurations in a bundle or rope^[15] and their electronic properties.^[16] Herein, we present and discuss the experimental characterization of the radial mechanical properties of single-walled BNNTs (SW-BNNTs) by using atomic force microscopy (AFM). Our results show for the first time that the effective radial elastic moduli of SW-BNNTs expectedly decrease with an increase in tube diameter, and are relatively lower than those of single-walled CNTs (SWCNTs) of the same diameter.

M. Zheng, X. M. Chen, Prof. C. H. Ke
Department of Mechanical Engineering
State University of New York at Binghamton
Binghamton, NY 13902, USA
E-mail: cke@binghamton.edu

Dr. I.-T. Bae
Small Scale Systems Integration and Packaging Center
State University of New York at Binghamton
Binghamton, NY 13902, USA

Dr. C. Park
National Institute of Aerospace
Hampton, VA 23666, USA

DOI: 10.1002/sml.201100946

Dr. C. Park
Department of Mechanical and Aerospace Engineering
University of Virginia
Charlottesville, VA 22904, USA

Dr. M. W. Smith
NASA Langley Research Center
Hampton, VA 23681, USA

K. Jordan
Thomas Jefferson National Accelerator Facility
Newport News, VA 23606, USA



2. Results and Discussion

The employed BNNTs were synthesized by using a novel pressurized vapor/condenser method.^[17] As-grown BNNTs, originally in the form of dry cottonlike fibrils, were separated in deionized water by ultrasonication with the aid of ionic surfactants.^[18] After centrifugation, small drops from the top portion of the BNNT solution were deposited on clean Si wafers and air-dried for AFM measurements, as well as on copper grids with lacy support films (Ted Pella, Inc.) for high-resolution transmission electron microscopy (HRTEM) measurements. Our inspection of BNNT samples using a JEM 2100F HRTEM instrument captured SW-BNNTs with diameters in the range of 0.6 to 2.4 nm, which is similar to that of SWCNTs and is exemplified by the tube (2.4 nm in diameter) in the HRTEM image shown in **Figure 1a**. A high-resolution AFM

instrument with closed-loop feedback control features in the motion along the *XYZ* axes (model XE-70, Park Systems) was employed for all the topography and mechanical measurements presented herein. **Figure 1b** shows a representative AFM topography image of one SW-BNNT with a tube cross-sectional height (h_0) of 1.92 nm, recorded in tapping mode using a silicon AFM probe (model T-190, VistaProbe). The diameter of this tube (D_{nt}) is estimated to be about 1.58 nm by considering $D_{nt} = h_0 - t$,^[19] in which $t = 0.34$ nm is the interlayer distance of the BN sheet.^[17] **Figure 1c** illustrates the atomic structure of a zigzag (20, 0) SW-BNNT (1.59 nm in diameter, side view), a possible structural architecture for the tube shown in **Figure 1b**.

Radial mechanical deformations of individual SW-BNNTs like the one shown in **Figure 1b** were characterized using AFM-based compression testing techniques, which were previously employed for studying the radial elasticity of single- and multi-walled CNTs.^[19–24] As illustrated by the inset drawing in **Figure 2**, a silicon tip on a silicon AFM cantilever (model CSG 11, NT-MDT) is controlled to scan an individual SW-BNNT on the substrate in contact mode at a specified constant compressive load with the scanning direction perpendicular to the tube axis. The employed AFM scanning rate and scanning length were 50 nm s^{-1} and 600–800 nm, respectively. All measurements were performed at room temperature. The actual spring constant of each employed AFM cantilever was calibrated using the thermal tuning method based on equipartition theory,^[25,26] and was found to be in the range of $0.04\text{--}0.09 \text{ N m}^{-1}$. The thermally induced root-mean-square (rms) deflection noise of the employed AFM probes at the tip position in the 1–500 Hz bandwidth was measured to be 0.71 \AA , and the corresponding rms force noise was calculated to be about 3–7 pN. The applied compressive load P is determined by the product of the spring constant of the AFM probe and its vertical deflection. The closed-loop feedback control feature of the employed AFM

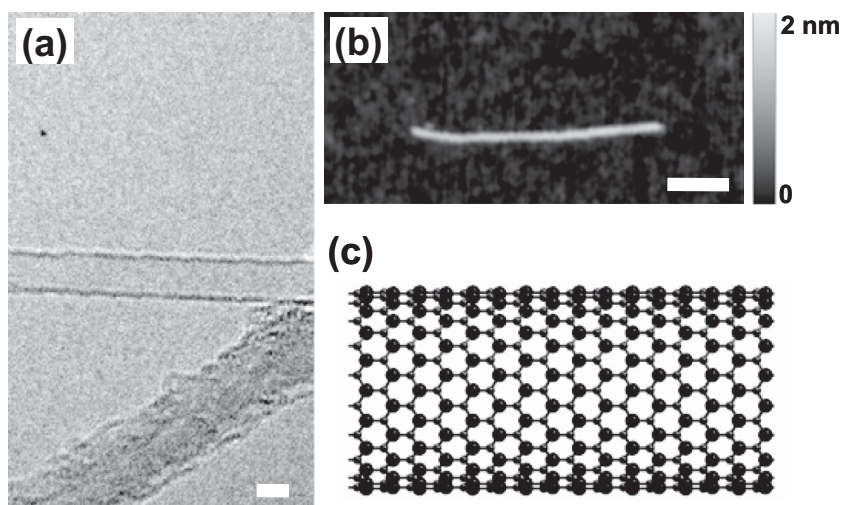


Figure 1. a) HRTEM image of one SW-BNNT with a diameter of 2.4 nm. b) AFM image of one SW-BNNT with a diameter of 1.58 nm. c) Schematic drawing of one zigzag (20, 0) SW-BNNT (1.59 nm in diameter, side view). The larger dots in the drawing represent nitrogen (N) atoms, while the smaller dots represent boron (B) atoms. The scale bars in (a) and (b) represent 2 and 100 nm, respectively.

enables angstrom-level positioning resolutions, and allows repeated contact-mode scanning of the same position on one SW-BNNT at a variety of compressive loads. The radius of curvature (R_{tip}) of the employed AFM tips is estimated to be $\approx 25 \text{ nm}$ based on the geometrical deconvolution relationship $R_{tip} = \omega^2/8\Delta$, in which Δ and ω are the measured height and apparent width of a nanotube in the captured AFM images, respectively.^[27] In the following data analysis and results discussion, the tested SW-BNNTs are assumed to undertake circular cross sections on the substrate, thus neglecting the effect of van der Waals interactions between the tube and the

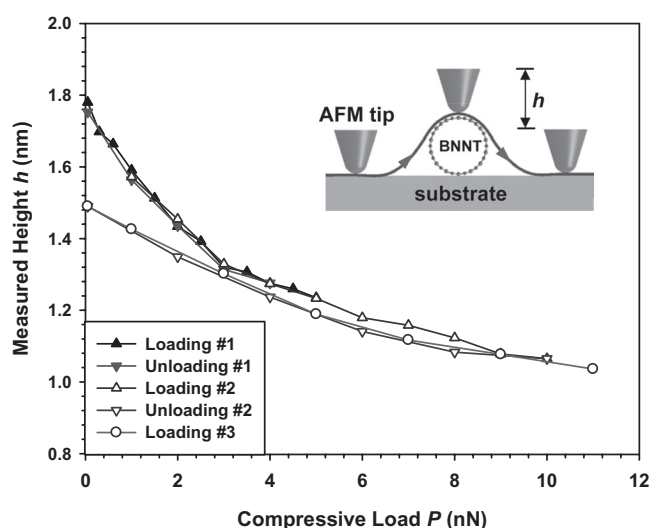


Figure 2. Repeated loading and unloading curves recorded on one SW-BNNT with an original tube height of 1.78 nm under ceiling compressive loads of 5 and 10 nN, respectively. Purely elastic behavior is displayed for the ceiling load of 5 nN by the first loading and unloading curves and the second loading curve. The inset drawing (not to scale) illustrates the AFM-based compression testing scheme on the radial deformation of an individual BNNT on a flat substrate.

substrate on flattening the tube cross section.^[28] The original height of the tested SW-BNNT on the substrate, h_0 , is estimated through power-function fitting and interpolation of the measured height h to zero load.

The radial deformations of individual SW-BNNTs were characterized through repeated compression and decompression measurements using AFM. The plotted curves in Figure 2 show the representative loading and unloading force–height profiles recorded on one SW-BNNT with $h_0 = 1.78$ nm for two levels of ceiling compressive loads at 5 and 10 nN, respectively (see Figures S1 and S2 in the Supporting Information for the force–height profile measurements). The good overlapping of the loading and unloading profiles for applied compressive loads up to 5 nN demonstrates that the tested SW-BNNT behaved elastically under the applied load, with the corresponding height reduction up to 30.6% of the original height. It is noted that the measured height reduction is ascribed to not only the radial deformation of the BNNT, but also the deformations of the AFM tip and the substrate. The measured height reduction reached 40.2% when the compressive load reached 10 nN (loading curve #2). The subsequent decompression process, represented by unloading curve #2, reveals a permanent height reduction of 15.3%, thus implying noticeable plasticity in the radial deformation of the tube at a compressive load of 10 nN. It is noticed that loading curve #3 follows the same path as unloading curve #2, which is a clear indication of the strain hardening effect during the plastic deformation under the 10 nN load. More prominent plasticity in the BNNT radial deformation was observed at higher radial compressive loads. Our measurements on one SW-BNNT with $h_0 = 0.92$ nm witnessed a 30.4% permanent height reduction when a compressive load of 20 nN was applied. The measured permanent height reduction indicates significant flattening of the tube cross section where the upper and lower portions of the tube cross section were essentially in close contact and held together by their van der Waals interactions.

The radial deformation behaviors, as shown in Figure 2, have been consistently observed on other tubes tested using the same testing scheme. The observed elastic deformational behaviors suggest that the relatively small strains induced by radial compression can be accommodated by the bending, rotation, and stretching of the B–N bonds in the SW-BNNT. Due to the partially ionic feature of the B–N bonding, large deformations of the B–N bond may lead to significant structural defects (e.g., bond breaking^[29]) and create energetically unfavorable homopolar B–B and N–N bonds, which weaken the local defect area and lead to plastic deformational behaviors.^[30] It is noted that the tested SW-BNNTs remained at a standstill on the substrate during the AFM scanning process within the above force ranges, presumably due to their van der Waals interaction-based adhesion with the substrate, which could be clearly identified from their consecutively recorded AFM scanning topography profiles (see Figure S1 in the Supporting Information).

By considering cylindrical hollow SW-BNNTs as elastic bodies, their effective radial elastic moduli ($E_{\text{nt}}^{\text{rad}}$) are expected to decrease with the increase in tube diameter.^[20,31] This is due to the fact that the strain energy in the tube is

inversely proportional to the tube diameter square. It is worth mentioning that the effective radial modulus in our model is different from the regular radial modulus for one-dimensional nanostructures with solid cross sections, such as gold nanowires.^[32] The effective radial moduli of the tested SW-BNNTs are interpreted using a Hertzian model by considering an elastic nanoindentation system consisting of a spherical tip, a cylindrical tube, and a flat substrate. The measured height of a SW-BNNT on the substrate under the compressive load P is given by:^[20]

$$h = h_0 - \left(\frac{P}{k_1 \sqrt{h_0}} \right)^{2/3} - \left(\frac{P}{k_2 \sqrt{R_*}} \right)^{2/3} + \left(\frac{P}{k_3 \sqrt{R_{\text{tip}}}} \right)^{2/3} \quad (1)$$

$$k_1 = \frac{4}{3} \left(\frac{1 - \nu_{\text{nt}}^2}{E_{\text{nt}}^{\text{rad}}} + \frac{1 - \nu_{\text{sub}}^2}{E_{\text{sub}}} \right)^{-1}, \quad k_2 = \frac{4}{3} \left(\frac{1 - \nu_{\text{tip}}^2}{E_{\text{tip}}} \right)^{-1},$$

$$k_3 = \frac{4}{3} \left(\frac{1 - \nu_{\text{tip}}^2}{E_{\text{tip}}} + \frac{1 - \nu_{\text{sub}}^2}{E_{\text{sub}}} \right)^{-1}$$

where E and ν represent the elastic modulus (effective radial elastic modulus for BNNTs) and Poisson's ratio, respectively, for materials of BNNTs (subscript nt), AFM tips (tip), and substrates (sub). The second term on the right side of Equation 1 represents the deformations of both the BNNT and the substrate due to the nanoindentation of the BNNT–substrate system. The third term represents the deformation of the AFM tip due to its contact with the BNNT (the BNNT is considered as a rigid body here to avoid double-counting its deformation). R_* is the reduced radius of curvature of the cylindrical tube–spherical tip system^[20,21] and is given by $R_* = [1/h_0 + 1/R_{\text{tip}}]^{-1}$. The last term represents the deformation of the substrate due to the nanoindentation of the AFM tip.

It is noted that the Hertzian model does not take into account the height deformations caused by the friction forces among all the elastic components, which are expected to be much smaller than the deformations caused by the compressive load. A native oxide layer of ≈ 2 nm was measured on the surface of the Si substrates using ellipsometry (Model Uvisel, Horiba Ltd.). Similar oxide layers are also expected on the surface of Si AFM tips.^[33] The materials for both the AFM tip and the substrate are considered to be native silicon oxide with an elastic modulus of 74 GPa and a Poisson's ratio of 0.16. Prior studies predict 0.13–0.41 for the Poisson's ratio of BNNTs^[34–36] and the value $\nu_{\text{nt}} = 0.2$ is considered in the present Hertzian model.

To ensure that the radial moduli of SW-BNNTs are properly calculated based on Equation 1, we employ the force–height profiles recorded during the initial compression process with a ceiling load of 5 nN or lower, where the radial deformations of SW-BNNTs are considered to be purely elastic. **Figure 3a** shows the radial deformation profiles (load versus height) for three selected SW-BNNTs with original heights on the substrate (h_0) of 0.92, 1.78, and 2.44 nm, respectively. The dots represent the experimental measurements, while the solid- and dashed-line curves represent theoretical fittings based on the Hertzian model in Equation 1. It is remarkable that the experimental data for all three tubes

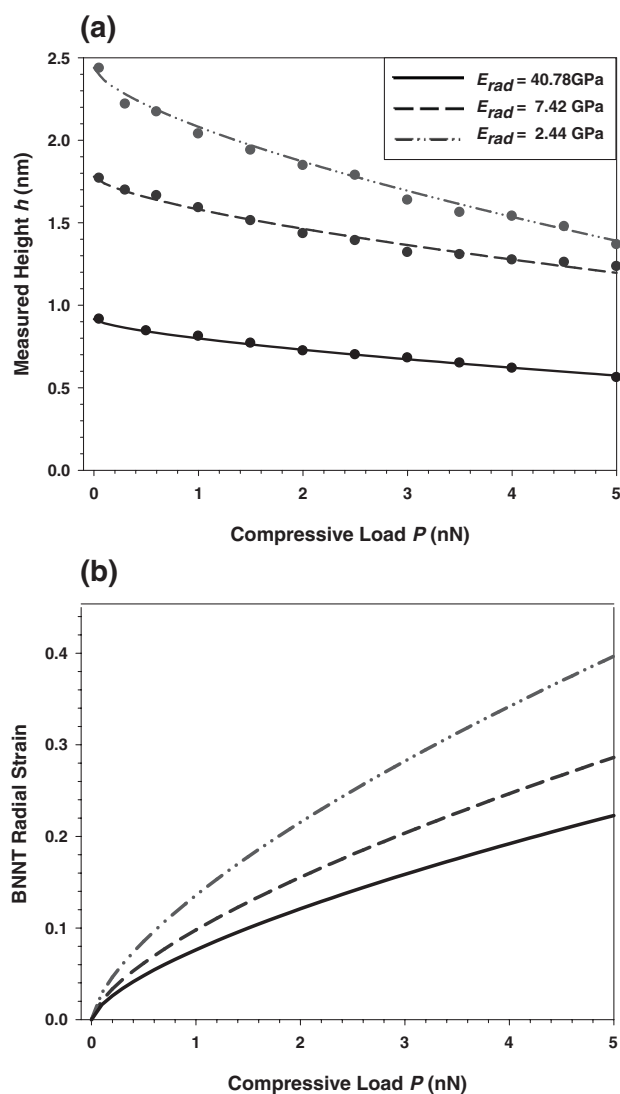


Figure 3. a) Force–height profiles for three selected SW-BNNTs. The dots represent experimental measurements, while the solid and dashed lines represent the fitting curves based on the Hertzian model. b) Theoretical prediction of the corresponding radial strain versus the compressive load for the three tubes shown in (a).

are well-fitted by the theoretical model. The effective radial elastic moduli of these three SW-BNNTs are calculated to be 40.78, 7.42, and 2.44 GPa, respectively, which expectedly decrease with the increase in tube diameter. The diametrical deformation of each tube along the load direction (δd) can be calculated based on Equation 1 by assuming that both the AFM tip and the substrate are rigid. Figure 3b shows the respective dependences of the radial strain $\varepsilon_{\text{nt}}^{\text{rad}}$, defined as $\varepsilon_{\text{nt}}^{\text{rad}} = \delta d/h_0$, on the applied load for the three SW-BNNTs shown in Figure 3a. Our results show that the radial strain at 5 nN for the tube shown in Figure 2 is 28.6%. Therefore the elastic radial deformation limit for this tube is likely to be within the range of 30–40%, which is smaller than previously reported values ($\approx 60\%$) for SWCNTs.^[19,20] The observed lower elastic limit of SW-BNNTs compared with SWCNTs is consistent with prior theoretical prediction that the elastic

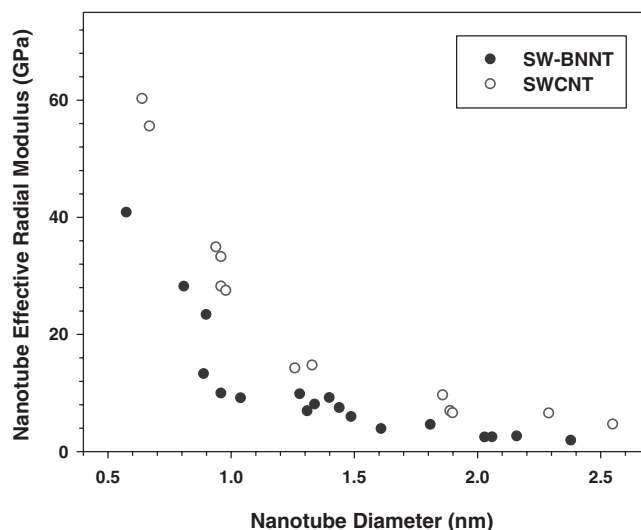


Figure 4. Comparison of the measured radial elastic moduli of SW-BNNTs (solid dots) and SWCNTs (open circles) as a function of nanotube diameter.

limit of SW-BNNTs is 20–40% smaller than that of SWCNTs as a result of differences in their high-stress-induced rotation and breaking of bonds.^[29,30]

Figure 4 shows the dependence of the measured effective radial elastic modulus of SW-BNNTs on the tube diameter for 18 different SW-BNNT samples, which clearly displays a decreasing trend of the effective radial elastic modulus with the increase in tube diameter. The measured effective radial elastic moduli of SW-BNNTs are found to range from 40.78 to 1.85 GPa for tube diameters in the range of 0.58 to 2.38 nm. Figure 4 also shows a comparison between SW-BNNTs and SWCNTs of their effective radial elastic moduli. The employed SWCNTs, synthesized by chemical vapor deposition (CVD) methods, were purchased from Cheap Tube, Inc., in the form of dried powders. The sample preparation, radial elasticity measurements, and data interpretation of SWCNTs were implemented using the same protocols and approaches as those employed for SW-BNNTs, except that $\nu_{\text{nt}} = 0.17$ is assumed for SWCNTs^[20] in the Hertzian model. It is noted that our measured effective radial elastic moduli of SWCNTs are consistent with previously reported experimental data^[20] and theoretical predictions^[37] (see Figure S3 in the Supporting Information). Our results consistently show that SW-BNNTs have relatively lower effective radial elastic moduli than SWCNTs of the same diameter.

The observed difference in the radial rigidity of SW-BNNTs and SWCNTs can be ascribed to several factors. First, SW-BNNTs are composed of partially ionic B–N bonds, compared with covalent sp^2 C–C bonds in SWCNTs. Prior theoretical work has demonstrated that the strain energy in SW-BNNTs is lower than that of comparable SWCNTs.^[34,35,38] In particular, during the radial compression, the adiabatic deformation of the C–C bond distributes the applied load much more effectively than the relatively localized B–N bond. Second, the previously observed unique surface buckling phenomenon for SW-BNNTs (does not occur for SWCNTs),^[34,39]

which is ascribed to the slight difference in the hybridization of B and N atoms in the B–N hexagonal network, may contribute to the weakening of the radial rigidity of SW-BNNTs. Third, the zigzag configuration, favorable for SW-BNNTs,^[40] is symmetric and thus deforms more readily than the asymmetric chiral architecture, which would be more probable for SWCNTs. Fourth, BNNTs reportedly have stronger van der Waals interactions with silicon substrates than CNTs,^[41] which undoubtedly tend to induce more prominent cross-section flattening for SW-BNNTs than comparable SWCNTs. This van der Waals interaction-induced nanotube cross-section deformation effect becomes particularly significant for tubes with large diameters.^[28] However, quantitative evaluation of the effect of the van der Waals interactions on the radial rigidities of SW-BNNTs and SWCNTs requires further investigation using advanced atomistic-level modeling techniques. Lastly, variations in the parameters and assumptions used in the calculation of the effective radial modulus, such as Poisson's ratio, also contribute to the observed difference in effective radial elastic modulus.

Because the radial rigidity of nanotubes is an important parameter in determining their configurations in nanotube bundles or ropes, the relatively weaker radial rigidity of SW-BNNTs suggests that they will more readily undertake hexagonal cross sections in bundles than SWCNTs,^[15] which may lead to more tightly bound nanotube fibers and yarns. In addition, SW-BNNTs will be energetically more favorable for large-angle bending and buckling than SWCNTs. Having Young's moduli comparable to SWCNTs, SW-BNNTs, either in the form of individual tubes or bundles, are compelling for applications demanding strong but supple structures. One such example is nanotube-based ceramic nanocomposites,^[13,42] where better conformation of nanotubes to ceramic grains is desired for fracture toughness improvement while providing higher-temperature process (e.g., sintering) environments. Combined with their superior high-temperature performance^[43] and electrically insulating properties, BNNTs are ideal for applications demanding high strength, thermal and chemical stability, and electrically insulating materials.

3. Conclusion

We have presented an AFM-based nanomechanical characterization of the radial mechanical properties of SW-BNNTs. Our measurements captured both elastic and plastic radial deformational behaviors of individual SW-BNNTs. Our work reveals that SW-BNNTs have a relatively lower rigidity in the transverse direction than SWCNTs, even though their longitudinal rigidities were reported to be comparable. The axially strong, but radially supple, characteristics of SW-BNNTs suggest that they may be superior to SWCNTs as reinforcing additives for nanocomposite applications. To the best of our knowledge, our study of the radial mechanical properties of SW-BNNTs is the first experimental work to be reported. Our results are useful for a better understanding of the mechanical properties of BNNTs and the pursuit of their potential applications.

Supporting Information

Supporting Information is available from the Wiley Online Library or from the author.

Acknowledgements

This work was funded by the US Air Force Office of Scientific Research Low Density Materials Program under Grant Nos. FA9550-11-1-0042 and FA9550-10-1-0451. This work was also partially supported by the American Chemistry Society–Petroleum Research Fund. The HRTEM imaging work was performed using the facilities in the Analytical and Diagnostics Laboratory at Binghamton University's Small Scale Systems Integration and Packaging Center (S³IP).

- [1] A. Rubio, J. L. Corkill, M. L. Cohen, *Phys. Rev. B* **1994**, *49*, 5081.
- [2] N. G. Chopra, R. J. Luyken, K. Cherrey, V. H. Crespi, M. L. Cohen, S. G. Louie, A. Zettl, *Science* **1995**, *269*, 966.
- [3] D. Golberg, Y. Bando, Y. Huang, T. Terao, M. Mitome, C. C. Tang, C. Y. Zhi, *ACS Nano* **2010**, *4*, 2979.
- [4] X. L. Wei, M. S. Wang, Y. Bando, D. Golberg, *Adv. Mater.* **2010**, *22*, 4895.
- [5] N. G. Chopra, A. Zettl, *Solid State Commun.* **1998**, *105*, 297.
- [6] R. Arenal, M. S. Wang, Z. Xu, A. Loiseau, D. Golberg, *Nanotechnology* **2011**, *22*, 265704.
- [7] Y. Xiao, X. H. Yan, J. X. Cao, J. W. Ding, Y. L. Mao, J. Xiang, *Phys. Rev. B* **2004**, *69*, 205415.
- [8] Y. Chen, J. Zou, S. J. Campbell, G. Le Caer, *Appl. Phys. Lett.* **2004**, *84*, 2430.
- [9] D. Golberg, Y. Bando, K. Kurashima, T. Sato, *Scr. Mater.* **2001**, *44*, 1561.
- [10] X. Blase, A. Rubio, S. G. Louie, M. L. Cohen, *Europhys. Lett.* **1994**, *28*, 335.
- [11] C. H. Lee, M. Xie, V. Kayastha, J. S. Wang, Y. K. Yap, *Chem. Mater.* **2010**, *22*, 1782.
- [12] C. Y. Zhi, Y. Bando, T. Terao, C. C. Tang, H. Kuwahara, D. Golberg, *Adv. Funct. Mater.* **2009**, *19*, 1857.
- [13] D. Golberg, Y. Bando, P. Dorozhkin, Z. C. Dong, *MRS Bull.* **2004**, *29*, 38.
- [14] Y. B. Li, P. S. Dorozhkin, Y. Bando, D. Golberg, *Adv. Mater.* **2005**, *17*, 545.
- [15] M. J. Lopez, A. Rubio, J. A. Alonso, L. C. Qin, S. Iijima, *Phys. Rev. Lett.* **2001**, *86*, 3056.
- [16] X. D. Bai, D. Golberg, Y. Bando, C. Y. Zhi, C. C. Tang, M. Mitome, K. Kurashima, *Nano Lett.* **2007**, *7*, 632.
- [17] M. W. Smith, K. C. Jordan, C. Park, J. W. Kim, P. T. Lillehei, R. Crooks, J. S. Harrison, *Nanotechnology* **2009**, *20*, 505604.
- [18] J. Yu, Y. Chen, B. M. Cheng, *Solid State Commun.* **2009**, *149*, 763.
- [19] T. DeBorde, J. C. Joiner, M. R. Leyden, E. D. Minot, *Nano Lett.* **2008**, *8*, 3568.
- [20] Y. H. Yang, W. Z. Li, *Appl. Phys. Lett.* **2011**, *98*, 041901.
- [21] I. Palaci, S. Fedrigo, H. Brune, C. Klinke, M. Chen, E. Riedo, *Phys. Rev. Lett.* **2005**, *94*, 175502.
- [22] A. P. M. Barboza, H. Chacham, B. R. A. Neves, *Phys. Rev. Lett.* **2009**, *102*, 025501.
- [23] M. F. Yu, T. Kowalewski, R. S. Ruoff, *Phys. Rev. Lett.* **2000**, *85*, 1456.
- [24] W. D. Shen, B. Jiang, B. S. Han, S. S. Xie, *Phys. Rev. Lett.* **2000**, *84*, 3634.

- [25] E. L. Florin, M. Rief, H. Lehmann, M. Ludwig, C. Dornmair, V. T. Moy, H. E. Gaub, *Biosens. Bioelectron.* **1995**, *10*, 895.
- [26] C. Ke, M. Humeniuk, H. S-Gracz, P. E. Marszalek, *Phys. Rev. Lett.* **2007**, *99*, 018302.
- [27] C. T. Gibson, G. S. Watson, S. Myhra, *Scanning* **1997**, *19*, 564.
- [28] T. Hertel, R. E. Walkup, P. Avouris, *Phys. Rev. B* **1998**, *58*, 13870.
- [29] A. N. Enyashin, A. L. Ivanovskii, *Inorg. Mater.* **2006**, *42*, 1336.
- [30] P. H. Zhang, V. H. Crespi, *Phys. Rev. B* **2000**, *62*, 11050.
- [31] H. Y. Wang, M. Zhao, S. X. Mao, *Appl. Phys. Lett.* **2006**, *89*, 211906.
- [32] B. Wu, A. Heidelberg, J. J. Boland, *Nat. Mater.* **2005**, *4*, 525.
- [33] H. Souha, D. Viale, G. Weber, B. Gillot, *J. Mater. Sci.* **1989**, *24*, 1767.
- [34] E. Hernandez, C. Goze, P. Bernier, A. Rubio, *Phys. Rev. Lett.* **1998**, *80*, 4502.
- [35] V. Verma, V. K. Jindal, K. Dharamvir, *Nanotechnology* **2007**, *18*, 435711.
- [36] E. S. Oh, *Mater. Lett.* **2010**, *64*, 859.
- [37] W. H. Chen, H. C. Cheng, Y. L. Liu, *Comput. Mater. Sci.* **2010**, *47*, 985.
- [38] K. N. Kudin, G. E. Scuseria, B. I. Yakobson, *Phys. Rev. B* **2001**, *64*, 235406.
- [39] E. Hernandez, C. Goze, P. Bernier, A. Rubio, *Appl. Phys. A: Mater. Sci. Process.* **1999**, *68*, 287.
- [40] R. S. Lee, J. Gavillet, M. L. de la Chapelle, A. Loiseau, J. L. Cochon, D. Pigache, J. Thibault, F. Willaime, *Phys. Rev. B* **2001**, *64*, 121405.
- [41] J. H. Hsu, S. H. Chang, *Appl. Surf. Sci.* **2010**, *256*, 1769.
- [42] L. N. An, W. X. Xu, S. Rajagopalan, C. M. Wang, H. Wang, Y. Fan, L. G. Zhang, D. P. Jiang, J. Kapat, L. Chow, B. H. Guo, J. Liang, R. Vaidyanathan, *Adv. Mater.* **2004**, *16*, 2036.
- [43] T. Dumitrica, H. F. Bettinger, G. E. Scuseria, B. I. Yakobson, *Phys. Rev. B* **2003**, *68*, 085412.

Received: May 15, 2011
Revised: July 14, 2011
Published online: November 14, 2011